Efficient Trotting of Soft Robotic Quadrupeds

Dimuthu D. K. Arachchige, Tim Sheehan, Dulanjana M. Perera, *Graduate Student Member, IEEE*, Sanjaya Mallikarachchi, *Graduate Student Member, IEEE*, Umer Huzaifa, Iyad Kanj, and Isuru S. Godage

***Abstract*—Soft robots hold significant potential in legged locomotion due to their inherent deformability, enabling enhanced adaptability to various environmental conditions and the generation of diverse locomotion gaits. While various soft robots have been proposed for terrestrial locomotion, research on dynamically-stable locomotion, such as trotting, with actuated soft bending limbs remains limited. We introduce a pneumatically-actuated soft quadruped featuring a soft body capable of a variety of dynamically-stable trotting locomotion. We utilize soft limb kinematics and parameterize fundamental limb locomotion to obtain quadrupedal locomotion trajectories for both linear and curvilinear motions. We also employ a physics-enabled dynamic model to optimize and evaluate trotting locomotion trajectories for dynamic stability. We further validate the stable locomotion trajectories through empirical experiments conducted on a soft quadruped prototype. The results demonstrate that the quadruped trots at a peak speed of 1.24 body lengths per second when traversing flat and uneven terrains, including slopes, cluttered areas, and naturalistic irregular surfaces. Furthermore, we compare the energy efficiency between trotting and crawling locomotion. The findings reveal that trotting is significantly more energy-efficient than crawling, with an average energy saving of up to 42%.**

***Note to Practitioners*—This paper was motivated by the challenge of achieving dynamically stable and efficient locomotion in soft quadrupeds. Many soft-legged robots are typically designed for statically stable, albeit inefficient and slow, locomotion gaits such as crawling. Our research aims to address this practical challenge of improving mobility in soft-legged robots. We develop a novel soft quadruped with pneumatically-actuated soft limbs that achieves efficient trotting that is 42% more energy-efficient than crawling. This work is particularly relevant for industries requiring adaptable and efficient navigation in environments, such as search and rescue, agricultural monitoring, and exploration. The development and optimization of trotting gaits through a physics-enabled dynamic model for dynamic stability provide a foundational framework for enhancing the adaptability and operational utility of soft robots. While our findings mark a significant step forward, challenges remain in deploying these locomotion strategies on autonomous untethered robots with onboard sensor feedback. Future research will focus on these areas, aiming to improve the practical deployment and robustness of soft robotic locomotive systems.**

***Index Terms*—Dynamically-stable locomotion, kinematics, PyBullet, soft quadrupedal robot, trotting.**

I. INTRODUCTION

MANY terrestrial vertebrates use legged locomotion as a prevalent mode of mobility. Their compliant musculoskeletal limbs can actively or passively strain and relieve muscle tension to absorb impact and adapt to unstructured terrains. Similar to biological creatures, soft-legged robots can absorb ground impact using active or passive compliance of soft legs. On the contrary, rigid-legged robots require separate or additional mechanisms to regulate impact and adapt to the environment. Soft robots are less likely to get damaged during an accident (e.g., falling) than rigid robots due to their ability to resile impulse forces using compliant structures [1]. In addition, these robots possess high levels of flexibility, agility, and maneuverability compared to their rigid-legged counterparts. Further, they are capable of deforming into smaller profiles and traveling through narrow spaces [2]. Hence, there is a strong prospect in employing soft-legged robots for activities, including search-and-rescue operations, inspections, space and underwater exploration, surveillance [3]. However, locomotion of soft-legged robots remains an area that has not reached its potential, hindered by various challenges such as inadequate deformation range, degrees of freedom (DoF), stiffness range (or strength), and control methods [4].

To date, most of the soft mobile robots utilize slow, statically stable gaits such as crawling [5]. Low-speed and locomotion inefficiency can be undesirable in certain field applications. Soft-limbed robots that were experimented with high-speed, dynamically stable locomotion gaits (e.g., trotting, galloping, etc.) are limited [6]. Researchers have tried to maintain locomotion stability by adding more limbs, i.e., soft hexapods use six limbs to bolster payload and attain statically stable gaits. However, more limbs increase the design and actuation complexity. Additionally, speedier gaits demand fewer limb-ground contacts. Consequently, with fewer limbs (4 instead of 6), there is a need for stronger legs to support the body

Received 7 August 2024; revised 18 December 2024; accepted 9 March 2025. Date of publication 20 March 2025; date of current version 2 May 2025. This article was recommended for publication by Associate Editor H. Su and Editor L. Zhang upon evaluation of the reviewers' comments. This work was supported in part by the National Science Foundation (NSF) under Grant IIS-2325491 (2008797), Grant CMMI-2326536 (2048142), and Grant CMMI-2327702 (2132994). *(Corresponding author: Dimuthu D. K. Arachchige.)*

Dimuthu D. K. Arachchige is with the School of Computing, Jarvis College of Computing and Digital Media, DePaul University, Chicago, IL 60604 USA, and also with the Department of Mechanical and Industrial Engineering, University of Illinois at Chicago, Chicago, IL 60607 USA (e-mail: DKODIP2@uic.edu).

Tim Sheehan, Umer Huzaifa, and Iyad Kanj are with the School of Computing, Jarvis College of Computing and Digital Media, DePaul University, Chicago, IL 60604 USA.

Dulanjana M. Perera and Sanjaya Mallikarachchi are with the Department of Multidisciplinary Engineering, Texas A&M University, College Station, TX 77843 USA.

Isuru S. Godage is with the Department of Engineering Technology and Industrial Distribution, the J. Mike Walker '66 Department of Mechanical Engineering (affiliated), and the Department of Multidisciplinary Engineering (affiliated), Texas A&M University, College Station, TX 77843 USA.

This article has supplementary downloadable material available at https://doi.org/10.1109/TASE.2025.3553082, provided by the authors.

Digital Object Identifier 10.1109/TASE.2025.3553082

weight. Nevertheless, most of the soft limbs proposed to date are found to be excessively pliant [7].

Soft limb deformation can be active or passive. Passively actuated soft limbs however reduce the effective DoF of the robot resulting in low dexterity. Actively bending soft limbs helps achieve dynamically-stable high-speed locomotion. Further, it enables squeezing through narrow spaces and obtain better locomotion maneuverability than passive limbs. However, to date, active bending soft-limbed robots have not resulted in meaningful dynamic gaits primarily due to inadequate structural strength of limbs [8].

A. *Related Work*

Soft mobile robots with various locomotion capabilities have been proposed [9]. This section categorizes the existing work into different types of soft-limbed robots, highlighting their achievements and limitations within the context of our proposed system.

Soft-limbed hexapods have garnered attention due to their statically stable locomotion. Suzumori et al. [10] pioneered pneumatically-actuated hexapods capable of omnidirectional mobility. Liu and Karydis [11] advanced this field by developing hexapods that could navigate rough and steep terrains. Li et al. [12] introduced untethered meter-scale soft hexapodal co-robots, and Hase et al. [13] utilized tetrahedral-shaped soft limbs for locomotion, showcasing innovative design. These studies highlight the versatility and adaptability of hexapods, although achieving high speeds and efficient maneuverability remains a challenge. Additionally, they suffer from design and actuation complexity due to the higher number of limbs.

Soft-limbed tetrahedral robots such as those reported in [14], [15], [16], and [17], achieved topple-free locomotion with statically-stable crawling gaits. Despite their stability, these robots were confined to low-speed gaits. The untethered soft robotic dog developed by Li et al. [18], demonstrated high-speed locomotion but struggled with turning maneuverability due to its relatively large rigid body. The "HSABot" [19] automated gait generation but was limited to low-speed walking. Similarly, soft bi-stable crawler [20] exhibited galloping but had passive limbs, which resulted in low maneuverability.

Several approaches have focused on soft quadrupedal robots. The cable-driven soft quadruped in [21] is capable of reaching targets while walking at low speed. The tortoise-inspired soft-limbed robots in [22] and [23] and the wheeler-leg soft-bodied robot in [24] were constrained to crawling. Similarly, the soft quadruped in [25] can self-amputate a limb when stuck but is limited to crawling. Pneumatically actuated soft quadrupeds in [7] and [8] have demonstrated multiple gait patterns, but the highly compliant limbs often resulted in slow locomotion and low efficiency. The untethered soft quadrupeds – "SQuad" [26] and "Flexipod" [27] replicated multiple locomotion gaits but lacked active bending and stiffness regulation capabilities due to their passive soft limbs being actuated only at the body-limb joints. The Gecko-inspired quadruped in [28] offered greater flexibility in turning due to their soft bodies but was limited to statically-stable gaits. Soft quadrupeds introduced in [29] and [30] featured tendon-driven variable compliance limbs but had limited workspace, affecting the variety of achievable gaits and speed. Similarly, soft quadrupeds in [31], [32], [33], and [34] have limited DoF limbs, resulting in statically-stable gaits at lower speeds and reduced maneuverability.

TABLE I

RECENT RESEARCH ON SOFT MULTI-LIMBED ROBOTS

Soft-limbed research	**Actuation method**	**Tethered?**	**Limb compliance**	**Dynamic stability?**	**Speed** $[BL/s]$
This quadruped, 2025	Pneumatic	Yes	Active	Yes	1.24
Tortoise-quadruped, 2025 [23]	Pneumatic	Yes	Active	No	0.41
Tumbling robot, 2024 [16]	Pneumatic	Yes	Active	No	0.65
Modular quadruped, 2024 [33]	Pneumatic	Yes	Active	No	0.21
Honeycomb robot, 2024 [34]	Pneumatic	Yes	Active	No	0.19
"Turbot" quadruped, 2024 [32]	Electric	No	Active	No	0.62
Self-amputating robot, 2024 [25]	Pneumatic	Yes	Active	No	0.11
Origami Quadruped, 2024 [30]	Electric	Yes	Active	No	0.28
Soft robotic dog, 2023 [18]	Electric	No	Active	Yes	0.97
"HSABot" quadruped, 2023 [19]	Electric	No	Active	No	0.04
Compliant crawler, 2023 [20]	Electric	No	Passive	Yes	1.56
Wheeler-legs robot, 2023 [24]	Pneumatic	Yes	Passive	No	0.42
"Tetraflex" robot, 2023 [17]	Pneumatic	Yes	Active	No	0.15
TSA hexapod, 2022 [13]	Pneumatic	Yes	Active	No	0.20
"BASR" quadruped, 2022 [22]	Pneumatic	Yes	Active	No	0.97
Tendon quadruped, 2022 [40]	Electric	No	Active	No	0.44
"Flexipod" quadruped, 2021 [27]	Electric	No	Passive	Yes	2.50
"OPARO" quadruped, 2021 [31]	Pneumatic	No	Active	No	0.11
Electronic-free robot, 2021 [37]	Pneumatic	Yes	Active	No	0.09

The shape memory alloy (SMA) actuated multi-limbed soft robot in [35] were constrained to low-speed crawling and statically-stable walking. The soft lithography-based multi-gait quadruped in [36] demonstrated crawling and undulation at low speeds. Furthermore, the soft quadruped in [37] featured limbs anchored to a central point on the body, leading to diminished stability during locomotion, while the quadruped in [38] showcased crawling and trotting locomotion, but its rigid body led to poor turning maneuverability. Our previous work [39] proposed a pneumatically actuated soft quadruped which was limited to statically stable crawling gaits.

To address the above limitations of the state-of-the-art, we extend the work [39] to investigate dynamically-stable trotting locomotion of soft quadrupeds. Table I compares the proposed work of this manuscript against most related soft-limbed robots in terms of various design aspects and locomotion capabilities. Note, to date, no soft-limbed robot that achieves dynamically stable locomotion at a speed higher than 1 body length per second (BL/s) using actively bending soft limbs has been proposed.

B. *Contributions*

The major contribution of this work is demonstrating an application of a physics-enabled modeling environment to optimize the gait parameters for feasible trotting locomotion in soft quadrupeds. A summary of our specific technical contributions is listed below.

i. Parameterize a fundamental limb motion using soft limb kinematics and derive jointspace trajectories for the trotting gait of soft quadrupeds.
ii. Develop an accurate real-time dynamic model of the soft quadruped in the PyBullet physics environment. The primary goal is to ensure realistic dynamic simulations

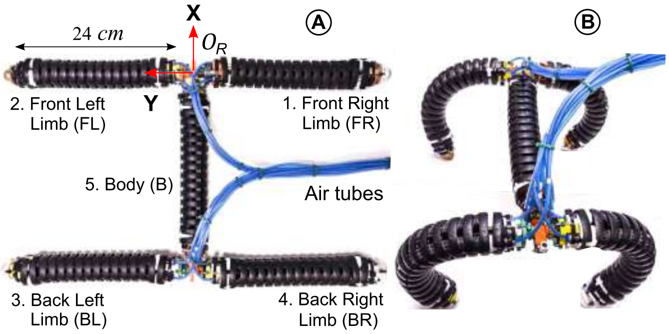

Fig. 1. Quadruped prototype in (A) unactuated and (B) locomotion poses.

TABLE II
QUADRUPED PROTOTYPE SPECIFICATIONS

Item	Detail
Soft limb (Fig. 2C)	Initial length, $L = 24\ cm$ Radius, $r = 2\ cm$ Bending ceilings, $\phi_j = [0, 180°]$ Bending stiffness at 325 kPa, $K_b = 1.18\ Nmrad^{-1}$ Damping coefficient at 325 kPa, $K_e = 730\ Nm^{-1}$ Mass, $m = 0.15\ kg$
Quadruped (Fig. 1A)	Body length, $L_M = 32\ cm$ Body width, $W_M = 54\ cm$ Body height, $h = 4\ cm$ Mass (without pressure supply tubes), $M = 0.85\ kg$

under dynamic characteristics such as gravity, damping, stiffness, friction, etc.

iii. Optimize and validate trotting locomotion trajectories on the physics engine-based quadruped model. The optimization occurs within the simulation model, demonstrating the feasibility and effectiveness of dynamically stable locomotion of the soft robotic quadruped with actively bending soft limbs.

iv. Validate the locomotion trajectories on the quadruped prototype based on optimized gait parameters of the physics-based model. We compare the performance of the robot prototype against the simulation model to demonstrate how closely the behavior of the physical robot aligns with the simulation model. To date, this is among the fastest tethered/untethered soft-limbed robot that demonstrates dynamically stable locomotion using actively bending soft limbs (refer to Table I).

v. Evaluate and compare the energy efficiency of trotting and crawling locomotion gaits. The energy consumption data shows that trotting is an energy-efficient mode of locomotion than previously reported crawling locomotion of the same quadruped [39].

II. SYSTEM MODEL

A. Quadruped Design

The quadruped shown in Fig. 1 is assembled using five identical soft modules, identified as Front Right (FR), Front Left (FL), Body (B), Back Left (BL), and Back Right (BR) limbs. A soft module mainly consists of a rigid, chain-link backbone and pneumatic muscle actuators (PMAs). PMAs are made of silicone tubes, union fittings and cable sleeves (Fig. 2A). To improve the actuation bandwidth a smaller-diameter silicone tube (11 mm internal diameter) is chosen. Three PMAs are placed inside an inextensible multi-axis cable carrier (i.e., backbone – Fig. 2B). PMAs are firmly fixed to either end of the backbone using 3D-printed parts highlighted in Fig. 2C. Fabrication details of PMAs and soft modules are given in [41]. This hybrid design, incorporating both stiff and soft materials, enhances the achievable stiffness range while decoupling stiffness and pose control, thus preserving inherent compliance and improving structural strength [42], [43], [44], [45]. This is essential for supporting the weight of the robot when replicating dynamically-stable gaits. The assembling details of the quadruped are given in [39]. We opted for a symmetric planar limb arrangement (Fig. 1A) to utilize the optimal workspace of soft limbs. Table II summarizes the physical details of the unactuated robot.

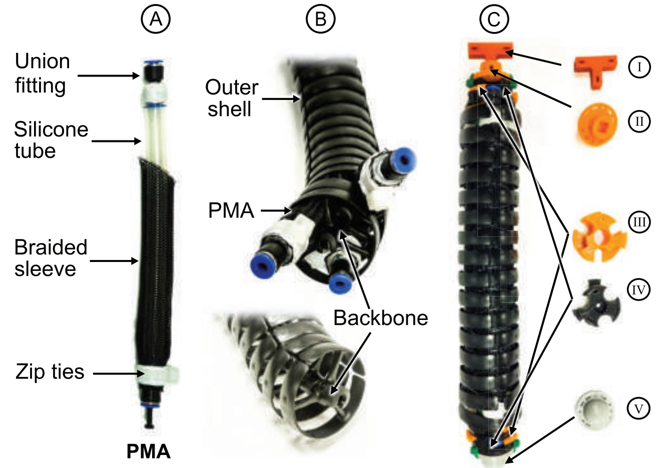

Fig. 2. Soft limb and its design elements: (A) a cross-section of Pneumatic Muscle Actuator (PMA), (B) PMA placement within the cable carrier (Igus Triflex TRL-40), (C) 3D-printed units: I - limb coupler, II - mounting base, III - PMA clamp, IV - connector cap, V - limb tip cap.

B. Soft Limb Kinematics

Without loss of generality, consider any j-th soft module or limb where $j \in \{1, 2, 3, 4, 5\}$. The origin of the coordinate frame, $\{O_j\}$ is fixed at the center of the base plate of j-th limb and a PMA is overlapped with the $+X_j$-axis as shown in Fig. 3A. The amount of pressure applied to any i-th PMA – $i \in \{1, 2, 3\}$ – during operation causes change of length $l_{ji} \in \mathbb{R}$ (i.e., joint variable). Assuming constant curvature deformation, the limb bending can be defined by curve parameters; orientation angle, $-\pi \le \theta_j \le \pi$ and the bending angle, $0 < \phi_j \le \pi$ [46]. Upon bending, the length of the i-th PMA can be expressed as $L + l_{ji}$, where L denotes the PMA's length when unactuated. Curve parameters and PMA lengths in Fig. 3A can be related to each other as given in [47] as

$$L + l_{ji} = \left\{ \frac{L}{\phi_j} - r\cos\left(\frac{2\pi}{3}(i-1) - \theta_j\right) \right\} \phi_j. \qquad (1)$$

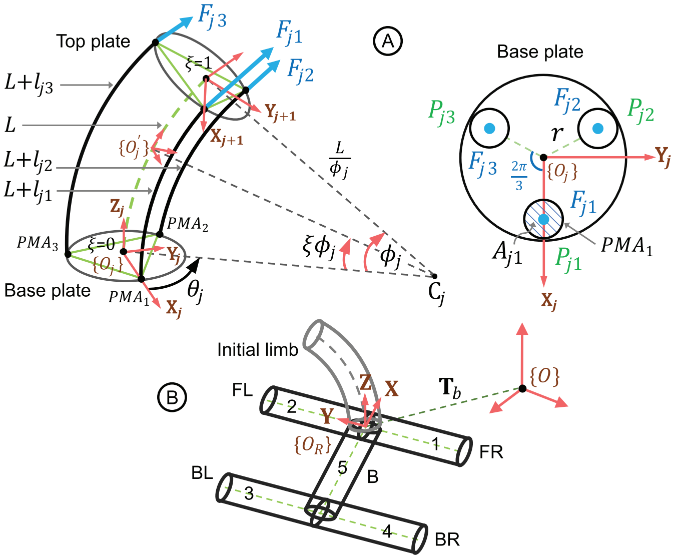

Fig. 3. Schematics of: (A) j-th soft limb illustrating curve parameters and pneumatic pressure forces exerted on the base plate, (B) quadruped.

The results in (1), can be utilized to obtain joint variable, l_{ji}, as

$$l_{ji} = -r\phi_j \cos\left(\tfrac{2\pi}{3}(i-1) - \theta_j\right). \tag{2}$$

The inextensible nature of the limb due to the backbone results in the kinematic constraint, $l_{j1} + l_{j2} + l_{j3} = 0$ [41]. Applying this kinematic constraint to (1), curve parameters can be derived in terms of two independent joint variables in the simplified form as

$$\phi_j = \tfrac{2}{\sqrt{3}r}\sqrt{l_{j2}^2 + l_{j3}^2 + l_{j2}l_{j3}}, \tag{3a}$$

$$\theta_j = \arctan\left\{\left(l_{j3} - l_{j2}\right), \sqrt{3}\left(l_{j2} + l_{j3}\right)\right\}. \tag{3b}$$

As detailed in [47], the complete homogeneous transformation matrix (HTM) of a j-th limb, $\mathbf{T}_j \in SE(3)$ is given by

$$\begin{aligned}\mathbf{T}_j(\boldsymbol{q},\xi) &= \mathbf{R}_Z(\theta_j)\,\mathbf{P}_X\left(\tfrac{L}{\phi_j}\right)\mathbf{R}_Y(\xi\phi_j)\,\mathbf{P}_X\left(-\tfrac{L}{\phi_j}\right)\mathbf{R}_Z(-\theta_j),\\ &= \begin{bmatrix}\mathbf{R}_j(\boldsymbol{q},\xi) & \mathbf{p}_j(\boldsymbol{q},\xi)\\ 0_{1\times 3} & 1\end{bmatrix},\end{aligned} \tag{4}$$

where $q = [\theta_j \quad \phi_j]^T$, and $\xi \in [0 \quad 1]$, determine a spatial point along the centerline of the limb. $\mathbf{R}_j$ and $\mathbf{p}_j$ denote homogeneous rotation and position matrices, respectively. From $\mathbf{p}_j$, the limb spatial location can be mapped to curve parameters as

$$x_j = L\phi_j^{-1}\cos\left(\theta_j\right)\left\{1 - \cos\left(\xi\phi_j\right)\right\}, \tag{5a}$$

$$y_j = L\phi_j^{-1}\sin\left(\theta_j\right)\left\{1 - \cos\left(\xi\phi_j\right)\right\}, \tag{5b}$$

$$z_j = L\phi_j^{-1}\sin\left(\xi\phi_j\right). \tag{5c}$$

Utilizing (5), the inverse kinematics of the soft limb can be obtained as presented in [39] as

$$\theta_j = \arctan\left(y_j, x_j\right), \tag{6a}$$

$$\tfrac{1}{\phi_j}\left[1 - \cos\left(\phi_j\right)\right] = \tfrac{1}{L}\sqrt{x_j^2 + y_j^2}. \tag{6b}$$

C. Soft Limb Kinetostatics

Refer to the force, F_{ji}, exerted on the base plate due to the distributed pneumatic pressure, P_{ji} of PMAs, as depicted in Fig. 3B. An imbalance in pressure across PMAs generates a force disparity, leading to a net torque at the tip relative to $\{O_j\}$, inducing the bending of the limb. Following standard sign convention, the X, Y, Z components of the torque M_{ji}, generated by each F_{ji}, can be written as

$$M_{ji}|_X = 0F_{j1} + rF_{j2}\sin\left(\tfrac{\pi}{3}\right) - rF_{j3}\sin\left(\tfrac{\pi}{3}\right), \tag{7a}$$

$$M_{ji}|_Y = -rF_{j1} + rF_{j2}\cos\left(\tfrac{\pi}{3}\right) + rF_{j3}\cos\left(\tfrac{\pi}{3}\right), \tag{7b}$$

$$M_{ji}|_Z = 0. \tag{7c}$$

Assuming a uniform cross-sectional area A_{ji} exists in each PMA, then $F_{ji} = P_{ji}A_{ji}$ and, (5) can be further deduced as

$$M_{ji}|_X = \tfrac{\sqrt{3}A_{ji}r}{2}\left(P_{j2} - P_{j3}\right), \tag{8a}$$

$$M_{ji}|_Y = \tfrac{A_{ji}r}{2}\left(-2P_{j1} + P_{j2} + P_{j3}\right). \tag{8b}$$

Utilizing results in (8), the net bending torque which incorporates pneumatic actuation pressures, is expressed by (9), where K_b represents the bending stiffness.

$$M_{ji}|_{Net} = \sqrt{\left(M_{ji}|_X\right)^2 + \left(M_{ji}|_Y\right)^2} = K_b\phi_j. \tag{9}$$

The result in (9) is applied to actuate the soft limb simulation model in Sec. IV-B and subsequently map its behavior with the soft limb prototype.

D. Complete Kinematics of the Quadruped

The complete kinematic model of the quadruped (i.e., the soft limbs) relative to the robot coordinate frame, $\{O_R\}$ is given as in [39] as

$$\mathbf{T}_{Limb_1}(q,\xi) = \mathbf{R}_X\left(\tfrac{\pi}{2}\right)\mathbf{R}_Z\left(-\tfrac{\pi}{2}\right)\mathbf{T}_{init}(q,\xi), \tag{10a}$$

$$\mathbf{T}_{Limb_2}(q,\xi) = \mathbf{R}_X\left(-\tfrac{\pi}{2}\right)\mathbf{R}_Z\left(\tfrac{\pi}{2}\right)\mathbf{T}_{init}(q,\xi), \tag{10b}$$

$$\mathbf{T}_{Limb_5}(q,\xi) = \mathbf{R}_Y\left(-\tfrac{\pi}{2}\right)\mathbf{R}_Z(\pi)\,\mathbf{T}_{init}(q,\xi), \tag{10c}$$

$$\mathbf{T}_{Limb_3}(q,\xi) = \mathbf{T}_{Limb_5}\,\mathbf{R}_X\left(-\tfrac{\pi}{2}\right)\mathbf{R}_Z\left(\tfrac{\pi}{2}\right)\mathbf{T}_{init}(q,\xi), \tag{10d}$$

$$\mathbf{T}_{Limb_4}(q,\xi) = \mathbf{T}_{Limb_5}\,\mathbf{R}_X\left(\tfrac{\pi}{2}\right)\mathbf{R}_Z\left(-\tfrac{\pi}{2}\right)\mathbf{T}_{init}(q,\xi). \tag{10e}$$

where $\mathbf{T}_{init}(q,\xi)$ is the HTM of the initial limb given in (4).

When the robot is moving, $\{O_R\}$ is defined as a floating-base frame relative to a global coordinate frame, $\{O\}$ (refer Fig. 3B) as shown in [39] as

$$\mathbf{T}_b(q_b) = \begin{bmatrix}\mathbf{R}_b(q_b) & \mathbf{p}_b(q_b)\\ 0_{1\times 3} & 1\end{bmatrix}, \tag{11}$$

$$\mathbf{T}_{Limb_j}\left(q_b, q_j, \xi\right) = \mathbf{T}_b(q_b)\,\mathbf{T}_{Limb_j}\left(q_j, \xi\right). \tag{12}$$

Here, $q_b = [\alpha,\ \beta,\ \gamma,\ x_b,\ y_b,\ z_b]$ denotes global transformation parameters with $[\alpha,\ \beta,\ \gamma]$ and $[x_b,\ y_b,\ z_b]$ are angle and translation offsets between $\{O\}$ and $\{O_R\}$ frames, respectively. The complete kinematic model is used to obtain kinematic and dynamic simulations of the proposed locomotion gaits in subsequent sections.

TABLE III

TERMINOLOGY FOR GENERATING LOCOMOTION TRAJECTORIES

Symbol	Definition
ρ	Trajectory stride radius
φ	Stance angle
$\{x_0, y_0\}$	Trajectory origin relative to the limb origin
x_d	X distance to the trajectory origin from the limb origin
d	Z distance to the trajectory origin from the limb origin
d_g	Z distance to the ground spread from the limb origin
s	Ground spread
t_s	Stance time period
τ	Trajectory period
f	Limb actuation frequency
ϑ	Swing angle at time, t
D	Duty cycle
ω_d	Phase shift in diagonally opposite limb pairs
ω_{FR}, ω_{FL}	Phase shift of front right and left limbs
ω_{BR}, ω_{BL}	Phase shift of back right and left limbs
Δt	Time shift between diagonal limb pairs
k	Scalar that relates Δt into τ and t_s
ρ_O, ρ_I	Trajectory radii of outer and inner limbs while turning
A_O, A_I	Outer and inner turn curve lengths
s_O, s_I	Ground spreads of outer and inner limbs
ρ_{FL}, ρ_{FR}	Trajectory radii of front left and right limbs
ρ_{BL}, ρ_{BR}	Trajectory radii of back left and right limbs
ϕ_B	Robot's body bending while turning
d_O, d_I	Horizontal distance to ground spreads of outer and inner limbs from the corresponding limb origin

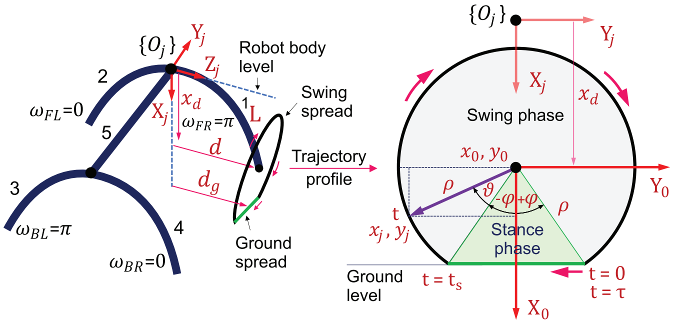

Fig. 4. Definitions of fundamental limb trajectory.

III. GENERATE TROTTING LOCOMOTION TRAJECTORY

A. Parameterize Fundamental Limb Motion

Without loss of generality, we derive a fundamental limb trajectory for one limb and, with appropriate phase shifts, apply to other limbs to generate quadrupedal locomotion. For clarity in the upcoming derivations, please refer to the notations outlined in Table III.

Herein, we consider that the limb heel follows the fundamental trajectory profile shown in Fig. 4. It is formed by a circular arc with a radius, ρ (swing phase) and a chord drawn at an angular offset, $\pm\varphi \in [0, \pm\pi]$ from the $+X_0$ axis of the trajectory (stance phase). We position the trajectory origin, $\{x_0, y_0\}$ at $\{x_d, 0, d\}$ relative to the limb's origin at O_j. Referring to notations in Fig. 4, the trajectory starts at time, $t = 0$ from the angular offset, $+\varphi$ and follows a clockwise direction with a period τ. The limb heel traces stance and swing phases at a uniform angular speed at time intervals, $0 \leq t < t_s$ and $t_s \leq t < \tau$, respectively. Herein, t_s defines the time period of the stance. The $X - Y$ projection of the taskspace of any j-th limb at time, t relative to $\{O_j\}$ can be obtained as

$$x_j = \begin{cases} x_0 + \rho\cos(\varphi), & 0 \leq t < t_s \\ x_0 + \rho\cos(\varphi + \vartheta), & t_s \leq t < \tau \end{cases} \tag{13}$$

$$y_j = \begin{cases} y_0 + \left(1 - \dfrac{2t}{t_s}\right)\rho\sin(\varphi), & 0 \leq t < t_s \\ y_0 - \rho\sin(\varphi + \vartheta), & t_s \leq t < \tau \end{cases} \tag{14}$$

where ϑ is the swing angle at time, t measured from $t = t_s$ in the clockwise direction during $t_s \leq t < \tau$.

The $Z-$component of the trajectory taskspace, z_j relative to the coordinate frame of the limb is given by (5c). However, given the limited kinematic DoFs of a soft limb, only the X, Y – components can be solved [39]. Hence we disregard the $Z-$component. The duty cycle, D, between the stance and swing phases can be defined as

$$D = \frac{t_s}{\tau}. \tag{15}$$

Considering uniform angular speed, ϑ can be deduced as

$$\vartheta = 2\pi\left(\frac{t}{\tau} - D\right). \tag{16}$$

Further, ground spread, s can be related to the trajectory stride radius, ρ as

$$s = 2\rho\sin(\varphi). \tag{17}$$

We discretize the limb taskspace trajectory, (x_j, y_j) into uniformly distributed 100 points within $[0, \tau]$ corresponding to the limb tip movement in Fig. 4. The taskspace is then transformed to a 100-point trajectory of curve parameters, (θ_j, ϕ_j) utilizing the inverse kinematics given in (6). Subsequently, we apply (1) to transform (θ_j, ϕ_j) into joint variables, l_{ji}. We use identical limb trajectories at each limb and actuate respective joint variables to achieve locomotion in the quadruped as described in Sec. III-B.

B. Generate Straight Trotting Locomotion

Trotting is a fast two-beat gait where diagonal limb pairs are lifted and struck the ground at π *rad* phase shift between each beat [48]. We achieve straight trotting locomotion by replicating the limb trajectory obtained in Sec. III-A with phase shifts, $\omega_{FR} = \omega_{BL} = \omega_d = \pi$ in FR, BL limbs and $\omega_{FL} = \omega_{BR} = 0$ in FL, BR limbs (Fig. 4). Accordingly, taskspaces of FR and BL limbs in (13) and (14) are modified as

$$x_{1,3} = \begin{cases} x_0 + \rho\cos(\varphi + \omega_d) & 0 \leq t < t_s, \\ x_0 + \rho\cos(\varphi + \vartheta + \omega_d) & t_s \leq t < \tau, \end{cases} \tag{18}$$

$$y_{1,3} = \begin{cases} y_0 + \left(1 - \dfrac{2t}{t_s}\right)\rho\sin(\varphi + \omega_d) & 0 \leq t < t_s, \\ y_0 - \rho\sin(\varphi + \vartheta + \omega_d) & t_s \leq t < \tau. \end{cases} \tag{19}$$

In order to maintain stability, we ensure that at least one diagonal limb pair is always at the stance phase, i.e., on ground during the stance-swing transition in a trajectory cycle. We achieve this by introducing a time shift, Δt such that $t_s = t_s + \Delta t$ letting a diagonal limb pair to initiate its limb trajectory with a

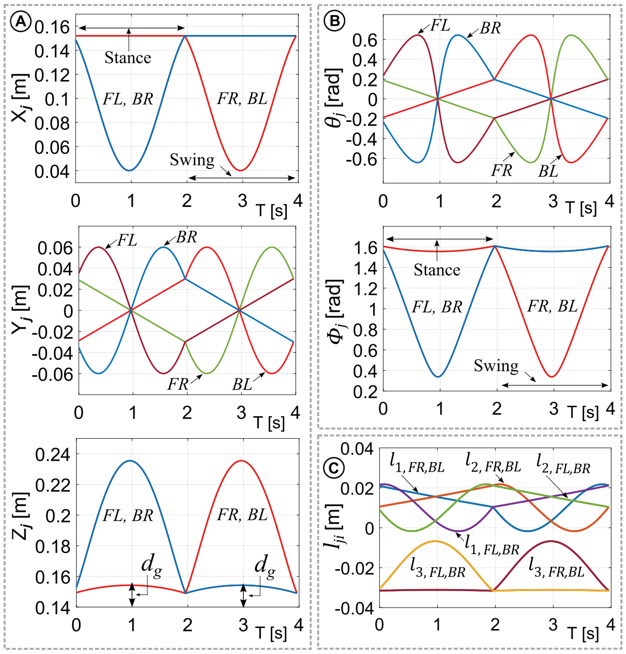

Fig. 5. Trajectory outputs: (A) $X - Y - Z$ taskspace, (B) curve parameters and, (C) joint variables of four limbs relative to individual coordinate frames of limbs, $\{O_j\}$ at $X_d = 10\ cm$, $\rho = 6\ cm$, $D = 0.2$, $\tau = 4\ s$, and $\Delta t = 1.34\ s$.

time delay relative to the other one. Note that, Δt depends on the limb actuation frequency, f (or trajectory period, $\tau = 1/f$) and stance period, t_s. Accordingly, to satisfy above ground contact requirement, we compute Δt as

$$\Delta t = \tau(k - D). \tag{20}$$

where $k\ (> D)$ is a scalar that relates Δt into τ and D based on limb trajectories of diagonal limb pairs.

During straight locomotion, the robot body is maintained at straight mode (i.e., $\theta_B = \phi_B = 0$) all the time. Figure 5 shows trajectory outputs (A – taskspace, B – curve parameters, and C – joint variables) of limbs in relation to their origins with $X_d = 10\ cm$, $\rho = 6\ cm$, $D = 0.2$, $\tau = 4\ s$ ($f = 0.25\ Hz$), and $\Delta t = 1.34\ s$. We verify the proposed locomotion trajectory through kinematic simulations performed in MATLAB. Please refer to Movie 01 of the accompanying multimedia file to see them.

C. Generate Turning Locomotion

For a given turn radius and a turn direction, we assume that the range of motion of a limb on the ground (i.e., ground spread) follows a turn curve as depicted in the rightward turn in Fig. 6A. The turning herein can be analogized to turning a four-wheeled automobile. Therein, inner and outer wheels follow turn curves with different radii. Since inner wheels follow a smaller turn curve, they make a tighter turn than outer wheels. We can replicate this phenomenon in the quadruped by giving different ground spreads for left and right limbs according to the desired turn direction and the turn radius. Note that, the ground spread, s is proportional to the trajectory stride radius, ρ as given in (17). Accordingly, in Fig. 6A, when trajectory radii of outer (or left) limbs are larger than the inner (or right) limbs (i.e., $\rho_O > \rho_I$ with $\rho_O = \rho_{FL} = \rho_{BL}$ and $\rho_I = \rho_{FR} = \rho_{BR}$), the robot moves in a rightward angular trajectory. Conversely, when the inner limb radii are larger, the robot turns leftward. When turning, we adjust the spatial deformation of the robot body, ϕ_B and $\theta_B = \pm\frac{\pi}{2}$, to match the turn angle. It prevents the robot from slipping sideways.

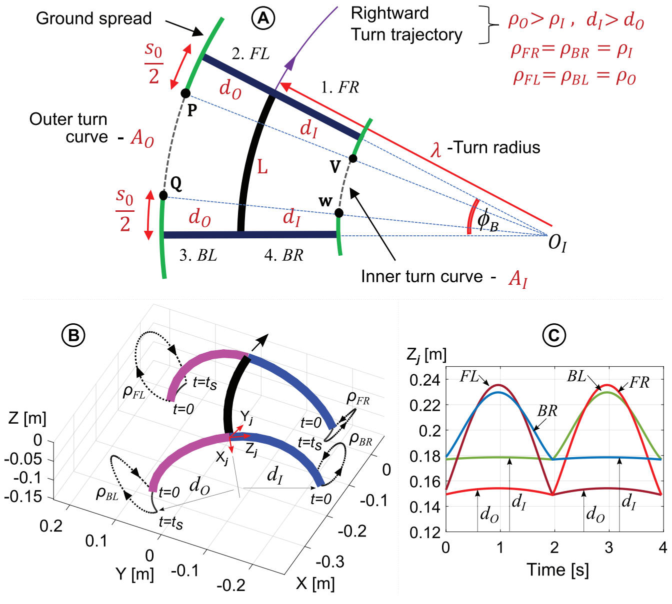

Fig. 6. (A) Modelling turning locomotion (rightward turn), (B) quadruped rightward turn with body bending and differential limb strides, (C) change in horizontal limb heel distance relative to $\{O_j\}$ according to differential limb strides.

Figure 6B spatially visualizes the aforementioned turning philosophy. The horizontal limb heel distance or distance to the ground spread relative to the corresponding body coordinate frame, $\{O_j\}$ (i.e., d_O or d_I in Figs. 6A and 6B) can be found from the trajectory taskspace, z_j (i.e., d_g in Fig. 5A) during the stance interval. For subsequent derivations, consider the notations in Fig. 6A. For known d_O, d_I and the desired turn radius, $\lambda(> d_O, d_I)$, the ratio between outer and inner turn curve lengths can be derived as

$$\frac{A_O}{A_I} = \frac{\lambda + d_O}{\lambda - d_I}. \tag{21}$$

By accounting ground spreads of outer limbs, s_0 and inner limbs, s_I, the length ratio between $P-Q$ and $V-W$ turn curves can be expressed as

$$\frac{A_O - s_0}{A_I - s_I} = \frac{\lambda + d_O}{\lambda - d_I}. \tag{22}$$

Results in (17), (21), and (22) relate the robot turn curve lengths to stride radii of two sides as

$$\frac{A_O}{A_I} = \frac{\rho_O}{\rho_I}. \tag{23}$$

Utilizing results in (21) and (23), we adjust the trajectory stride radii of two sides as

$$\rho_O = \left(\frac{\lambda + d_O}{\lambda - d_I}\right)\rho_I. \tag{24}$$

Additionally, the robot's body bending, ϕ_B can be adjusted as

$$\phi_B = \frac{L}{\lambda}. \tag{25}$$

Figure 6C shows the variation of the horizontal limb heel distance relative to $\{O_j\}$ based on different trajectory strides (ρ_O, ρ_I) of outer and inner limbs. We obtained those results by applying a turning radius, $\lambda = 40\ cm$ with $X_d = 10\ cm$, $D = 0.2$, $\rho_I = 4\ cm$, and $\tau = 4\ s$ $(f = 0.25\ Hz)$. Utilizing (24) and (25), we found $\rho_O = 6\ cm$ and $\phi_B = 37.2°$, respectively.

IV. SOFT QUADRUPED DYNAMIC MODEL

In trotting, diagonal pairs of limbs touch the ground alternately, which contributes to dynamic stability. Additionally, there exists a brief moment when all four limbs may simultaneously contact the ground, especially at lower speeds, providing a transition phase for increased stability. To facilitate the described movements, the robot needs to generate adequate momentum in the direction of motion [48]. This requirement should be rigorously evaluated under dynamic conditions to ensure optimal performance. The inherent hysteresis and nonlinearity of PMAs pose challenges in deriving gait trajectories for generating the required momentum, particularly within the constrained bandwidth of PMAs. Thus, an empirical approach becomes necessary. Implementing such an empirical approach directly on the physical robot is impractical due to the vast search space resulting from numerous parameters influencing its stability. In this context, we present the development of a comprehensive, physics-based real-time quadruped simulation model. This model allows us to optimize the parameterized trajectories to identify viable trajectories for subsequent testing on the actual robot proposed in Sec. III.

A. *PyBullet Physics Engine*

We employ PyBullet to develop a physics-enabled dynamic simulation model for the quadruped [49]. Serving as a Python wrapper for the popular Bullet physics engine [50], PyBullet facilitates the efficient simulation of rigid body dynamics, encompassing collisions, kinematic/dynamic constraints, friction, gravity, and other physics-based interactions. While PyBullet includes soft body modeling, its support is limited to simulations involving passive soft bodies, such as clothes, rubber, and foam [51]. Consequently, the development of a dynamic model for the quadruped with actively deforming soft limbs is not yet supported. However, previous studies have demonstrated that, with adequate discretization, lumped mass approaches offer a viable means to approximate actively deforming soft-bodied systems with sufficient accuracy [52], [53], [54]. Observing the use of mass-spring-damper approach in PyBullet to model soft bodies, we adopt a similar strategy to approximate a soft limb using rigid bodies for enhanced computational efficiency.

B. *Soft Limb and Quadruped Dynamic Models*

To model the soft limb, we adopt the discretization approach described in [52], approximating the limb as a series of 8 identical, equispaced discrete discs connected by revolute joints, as shown in Fig. 7A. The choice of 8 discs was informed by iterative testing, demonstrating that this number is sufficient to capture key characteristics of the physical limb prototype, such as the maximum bending angle, while balancing deformation fidelity and computational cost. The simulation model's physical and mechanical parameters such as mass, moment of inertia, stiffness, and damping, were tuned to match the behavior of the limb prototype. These parameters, detailed in Table II, were experimentally identified using a procedure outlined in our previous work [42]. We generate the XML-based URDF (Unified Robot Description Format) file for the discrete equivalent model which is then replicated, assembled in the quadrupedal configuration, and used within PyBullet dynamic simulation environment. We use two fixed joints to anchor four limbs to the body and assemble the quadruped PyBullet model shown in Fig. 7B. The limb trajectories that were implemented in MATLAB in Sec. III are imported to Python with the help of the MATLAB Engine API for Python [55].

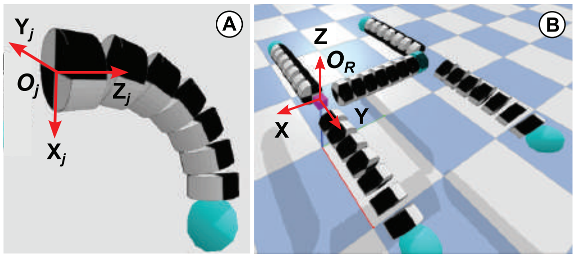

Fig. 7. A) Soft limb PyBullet model, B) quadruped PyBullet model.

For given curve parameters $(\theta_j, \phi_j$ in Sec. II), the two revolute joints are actuated via the position control mode in a sequential manner to manipulate the limb. In calculating ϕ_j, the bending torque defined in (9) is uniformly distributed across all revolute joints. In position control mode, PyBullet automatically computes and applies the relevant directional torque linked with θ_j to the revolute joints.

C. *Optimize and Validate Trotting Locomotion Trajectories for Dynamic Stability*

In this section, we iteratively test various locomotion parameters to identify dynamically stable trotting gaits. Note that the optimization is aimed at achieving stability in locomotion rather than efficiency.

We first characterized the PyButlet soft limb model to match the dynamic response of the soft limb prototype for the fundamental limb trajectory (Fig. 4) proposed in Sec. III. The testing procedure is outlined in Sec. V-B. Actuating pressure trajectories of the limb prototype are mapped to the bending torques applied in the limb simulation model using (9). We iteratively modified the bending stiffness and damping coefficients of the PyBullet limb dynamic model to optimize the dynamic trajectory tracking of the limb prototype. The resulting trajectories are shown in Fig. 8D. Next, we apply different combinations of stride radius (ρ), duty cycle (D), position of the trajectory origin relative to limb base (x_d), limb

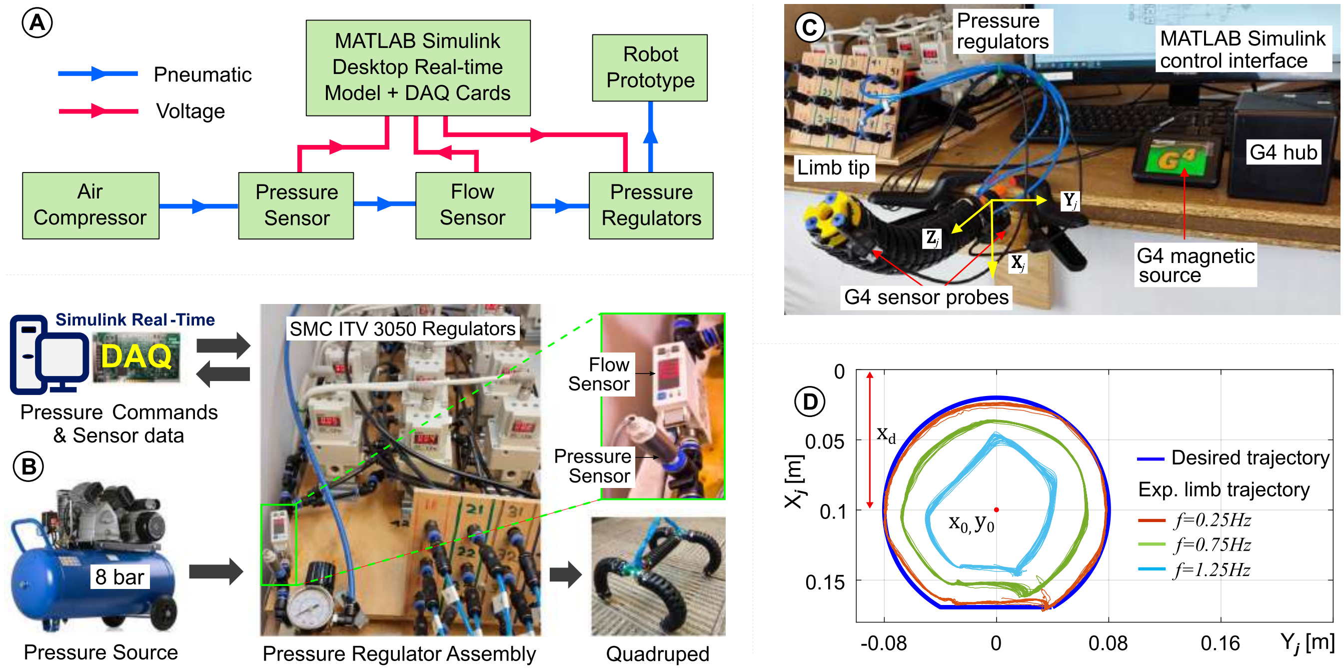

Fig. 8. (A) Block diagram and (B) components illustrating the actuation setup for the quadruped prototype. (C) Experimental setup for testing fundamental limb trajectory. (D) Recorded trajectory profiles of a soft limb prototype.

TABLE IV
GAIT PARAMETER GRID FOR PYBULLET SIMULATIONS

ρ $[cm]$	D	x_d $[cm]$	f $[Hz]$	Δt $[s]$
4.0	0.1	7.0	0.25	1.67
5.0	0.2	8.0	0.35	0.95
6.0	0.3	9.0	0.50	0.67
7.0	0.4	10.0	0.65	0.51
8.0	0.5	11.0	0.80	0.42
9.0			0.95	
10.0			1.25	

actuation frequency ($f = 1/\tau$ Hz), and time delay between diagonal limb pairs (Δt) derived in Sec. III, to obtain stable locomotion in the PyBullet quadruped dynamic model.

We set the friction coefficients of the simulation environment floor as, $\mu_x = \mu_y = 0.6$. They approximately match the friction coefficients of the actual floor (experimentally found in our previous work [56]), where the quadruped prototype will be tested. Based on the characterization and operating bandwidth of the soft limbs, we determined the testing range of the gait parameters as, $\rho \in [4, 10]$ cm, $D \in [0.1, 0.5]$, $x_d \in [7, 11]$ cm, and $f \in [0.25, 1.25]$ Hz. For the above parameters, from (20), the testing range of Δt was computed as $\Delta t \in [0.42, 1.67]$ s. We uniformly discretized each range and built the parameter grid shown in Table IV. Subsequently, we tested trotting performance via the quadruped dynamic model developed in Sec. IV-B for each parameter combination. The model started trotting approximately at $\rho = 6$ cm, $D = 0.1$, $x_d = 8$ cm, $f = 0.65$ Hz, and $\Delta t = 0.51$ s. We observed that the robot tends to slip at the specified friction. Hence, friction coefficients were slightly (approximately 8%) increased to improve the stability. A 8% increase in the friction coefficients could be a reasoned choice based on the need for a slight improvement in stability without significantly departing from realistic conditions.

This simulation study revealed that low limb actuation frequencies ($0.25 < f < 0.65$ Hz) led to unsuccessful trotting locomotion attempts. However, stability was maintained at a critical threshold of $f = 0.65$ Hz and beyond. The underlying cause for this behavior is the inadequacy of low limb actuation rates in generating the requisite forward momentum essential for sustaining dynamic stability during movement. We also noted that higher values of x_d (approximately 10 cm) contributed to improved trotting stability. This improvement stems from the effect of elevated x_d values causing limbs to pivot closer to the robot body, effectively redistributing mass and lowering both angular momentum and resultant torque generated by limb-ground reaction forces. This optimization aids in accurately tracking the gait trajectory while adhering to the assumption of constant curvature for limb bending. Conversely, lower values of x_d prompt a transition from trotting to crawling, as the limb tip extends farther from the robot body, aligning the trajectory origin (x_0, y_0) horizontally with the limb origin (O_j). Notably, the success of quadruped trotting was constrained within narrower margins of D $(0.1 < D < 0.3)$ and Δt $(0.42 < \Delta t < 0.67$ $s)$ due to their significant distortions of the original limb trajectory.

Top margins of ρ (> 10 cm) and x_d (> 11 cm) failed the trajectory generation (i.e., inverse kinematics failed) since they try to actuate the limb beyond its workspace. Table V gives the identified margins of each gait parameter that generated stable locomotion. Utilizing those optimized parameter margins, we tested the PyBullet dynamic model for turning trajectories proposed in Sec. III-C. Figures 9A and 11A show successive simulation frames of straight locomotion and turning, respectively. The complete PyBullet simulations are included in our multimedia file (Refer to Movie 02).

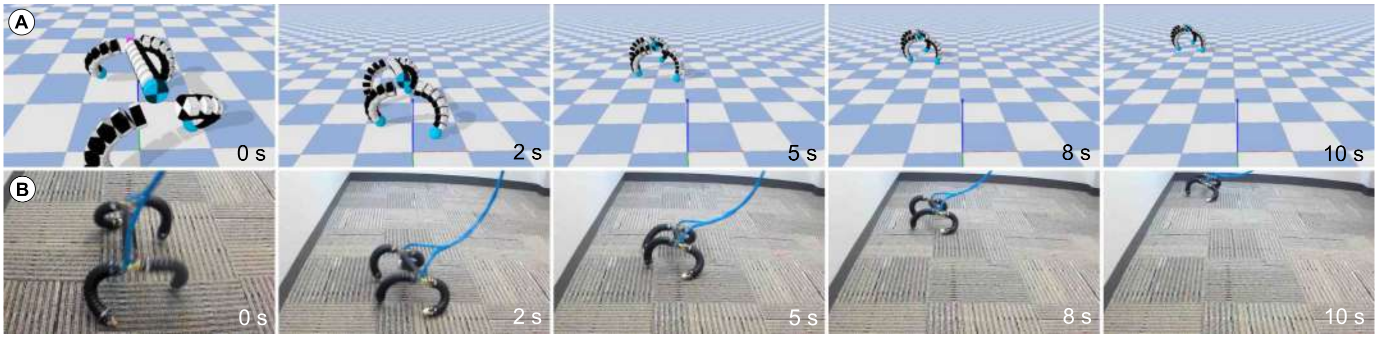

Fig. 9. Straight locomotion at $\rho = 6\ cm$, $D = 0.2$, $x_d = 10\ cm$, $f = 0.80\ Hz$, and $\Delta t = 0.42\ s$: (A) PyBullet simulation model, (B) quadruped prototype.

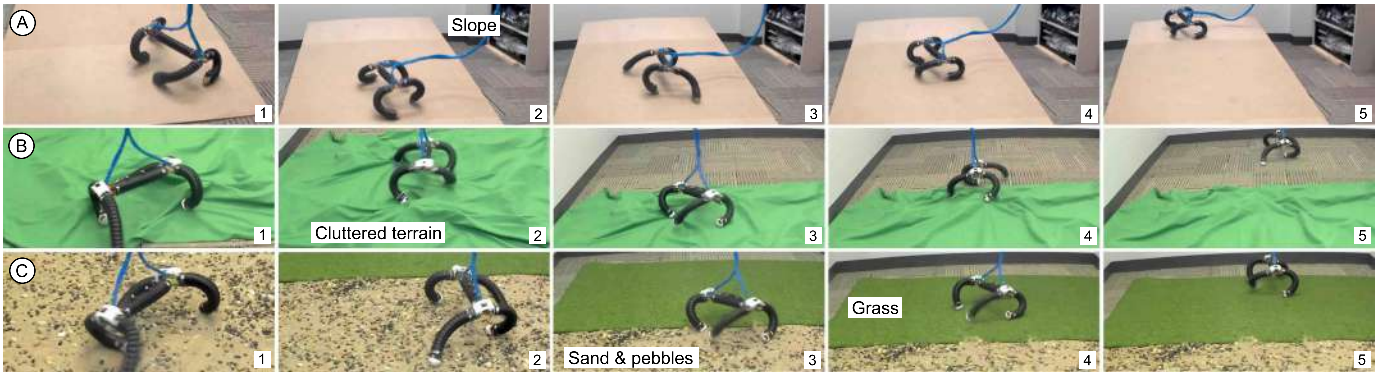

Fig. 10. Testing the quadruped prototype on various terrains: (A) inclined surface, (B) cluttered terrain (fabric with underlying obstacles), and (C) naturalistic uneven terrain (with sand, pebbles, and grass).

V. EXPERIMENTAL VALIDATION

A. Experimental Setup

The block diagram and hardware components of the experimental setup configured for the quadruped actuation are shown in Figs. 8A and 8B, respectively. A compressor with a constant pressure output of 800 kPa serves as the pressure supplier. Air pressure to each PMA of the soft limbs is controlled through a digital pressure regulator (ITV3050-31F3N3, SMC USA). The air inlet to the 15-unit pressure regulator assembly – corresponding to 15 PMAs in 4 limbs and the body – is monitored using serially coupled pressure and flow sensors. Input pressure commands to regulators are provided as voltage signals in the range $0-10\ V$ via an analog output data acquisition card (6703 PCI, NI USA) interfaced with a MATLAB Simulink Desktop Real-Time model. To actuate soft limbs and enable locomotion, joint variables (i.e., length trajectories such as those appeared in Fig. 5C) were converted into pressure trajectories and input via the pressure regulators in Fig. 8B. We employed the length-pressure mapping described in [39] to obtain pressure trajectories.

B. Test Fundamental Trajectory on a Limb Prototype

The limb trajectory introduced in Fig. 4 underwent experimental testing using the setup depicted in Fig. 8C. Initially, curve parameters (θ_j, ϕ_j) and joint variables (l_{ji}) were computed in accordance with the desired fundamental trajectory parameters ($\rho = 8\ cm$, $D = 0.2$, and $x_d = 10\ cm$), following the methodology outlined in Section III. Subsequently, the kinematic model in (4) was employed with θ_j and ϕ_j inputs to numerically derive the desired limb tip position $\{x_j, y_j\}$. This calculated trajectory was then transformed into pressure trajectories at the pressure ceiling of 300 kPa. The limb prototype shown in Fig. 8C was cyclically actuated at low, mid, and high frequency ranges ($f = \{0.25, 0.75, 1.25\}\ Hz$) independently over a duration of 20 s. During each actuation cycle, a motion tracker (6-DoF electromagnetic tracker, Polhemus G4 USA) recorded the spatial position of the limb tip $\{x_j, y_j\}$ relative to the limb' s origin. Fig. 8D showcases a comparison between numerically obtained and experimentally recorded limb tip positions. The observations indicate that the recorded limb trajectory closely aligns with the desired trajectory at low frequencies ($f < 0.25\ Hz$), undergoes contraction into smaller profiles at mid frequencies ($0.25\ Hz < f < 1.00\ Hz$), and experiences distortion at high frequencies ($f > 1.00\ Hz$). This distortion arises due to the phenomenon where rapid pressure changes lead to incomplete limb deformation. Additionally, it

TABLE V
OPTIMIZED GAIT PARAMETERS THROUGH PYBULLET SIMULATIONS

Gait parameter	Optimized region
Trajectory stride radius, ρ	$4-8\ cm$
Duty cycle, D	$0.1-0.3$
Distance to the trajectory origin, x_d	$8-10\ cm$
Limb actuation frequency, $f = 1/\tau$	$0.65-1.0\ Hz$
Time delay between diagonal limb pairs, Δt	$0.42-0.67\ s$

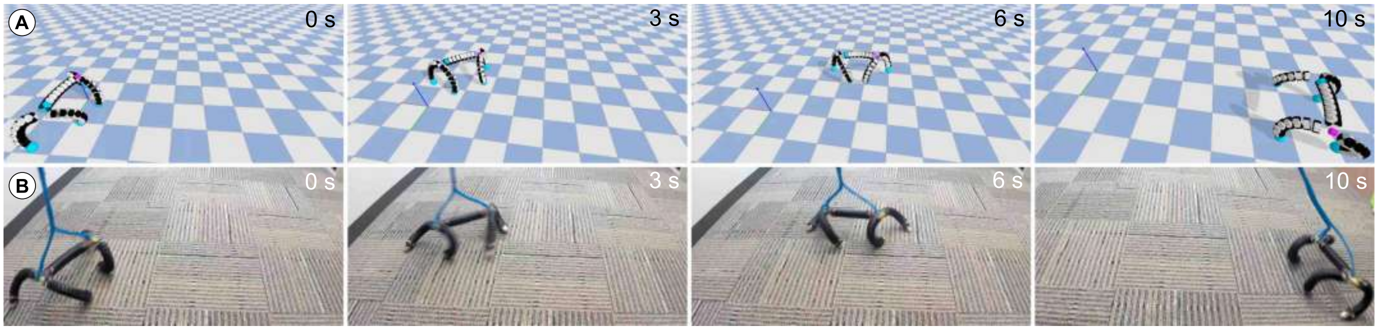

Fig. 11. Rightward turn at $\rho_I, \rho_O = 4, 6\ cm$, and body bending, $\phi_B = 37.2^\circ$ in (A) PyBullet simulation model, (B) quadruped prototype. Herein, trajectory parameters; D, x_d, f, and Δt unchanged from straight motion.

is worth noting that the employed kinematic model does not encompass factors such as deadzones, hysteresis, and gravity, which are associated with the behavior of the limb prototype. Consequently, the irregularities observed in the trajectory within Fig. 8D are to be expected across all instances.

C. Validate Straight Locomotion on the Quadruped Prototype

We used the optimized trajectory parameters in Table V as the baseline for the quadruped prototype testing. The quadruped was actuated for 10 s on a carpeted floor (see Fig. 9B). We initiated the locomotion in an unactuated pose where the quadruped is hanging at a certain distance above the ground. We used pressure supply tubes – bundled at the geometric center of the quadruped – to lift and keep the quadruped off the ground at the beginning. This pose ensures that the quadruped gained the initial stance force before locomoting, thereby facilitating stable and consistent ground contact across all limbs. It aids in stabilizing the quadruped' s initial posture, minimizing the risk of undesired slipping or misalignment during the transition to active movement. We estimated the desired hanging distance with the help of the limb trajectory given in Fig. 4. Therein, the hanging distance equals to the ground distance, $x_g = x_d + \rho\cos(\varphi)$ measured along the $+X_j$ axis relative to the limb' s origin at O_j. During locomotion, the pressure supply tube bundle is released and freely guided without impeding the robot movement (see experimental videos→Movie 03).

The testing was initiated at the lower ceiling of parameters listed in Table V and the pressure ceiling of $p = 300\ kPa$. Different combinations of trajectory parameters within their optimized regions and pressure ceilings were applied until the quadruped attained its steady locomotion. During straight movements, the quadruped body is kept at straight by supplying identical pressure ceilings onto its 3 PMAs. The best stable trotting locomotion was observed at $\rho = 6\ cm$, $D = 0.2$, $x_d = 10\ cm$, $f = 0.80\ Hz$, $\Delta t = 0.42\ s$ and $p = 325\ kPa$. Figure 9B shows its progression. Complete videos of several experimental trials are included in the multimedia file (Refer to Movies 03). The selection of the pressure ceiling relies on factors such as the characteristics of individually tailored PMAs, the entirety of the quadruped structure including the length of air supply tubes, limb actuating frequency, and so forth. We found that a low-pressure ceiling ($< 300\ kPa$) onto PMAs cannot provide adequate limb stiffness that can make the quadruped move while bearing its own weight. On the contrary, a high-pressure ceiling ($> 350\ kPa$) generated unexpected jerks due to over-stiffed limbs resulting in unsteady locomotion. The quadruped could not produce stable locomotion at the limb actuation frequency, 0.65 Hz recommended by PyBullet dynamic model due to inadequate forward momentum. Additionally, actuation frequencies above 1 Hz (i.e., during high-speed maneuvers) led to unstable movements, such as wobbling, due to the creation of incomplete limb trajectories. This instability arises because such frequencies surpass the operational bandwidth of PMAs. Refer to Movie 05 of the multimedia file to witness the above failure scenarios.

TABLE VI

Performance of Straight Locomotion

Model	**Speed** $[cm/s]$
Quadruped PyBullet model	44.4
Quadruped prototype	39.8
Error [%]	10.3

Table VI shows the recorded locomotion speeds of the PyBullet model and the quadruped prototype for straight motion under identical trajectory parameters. We utilized video feedback from front and overhead cameras, along with floor geometry, to estimate the robot's displacement on the X-Y plane. This estimation was achieved by employing an image projection method akin to the one described in [57]. According to the results in Table VI, the speed error between the two models is less than 11 %. Overall, quadruped models demonstrated fast locomotion gaits well.

Additionally, we expanded the robot prototype testing into uneven and irregular terrains, as depicted by Fig. 10, including slopes (inclination =40°), cluttered terrain (fabric with underlying obstacles), and naturalistic uneven terrain with obstacles such as sand, pebbles, and grass by applying optimized gait parameters from the PyBullet simulations. Our experimental results (See Movie 04) confirm the robot' s ability to locomote under these varied uneven conditions.

D. Validate Turning

We tested the quadruped turning by applying proposed turning trajectories in Sec. III-C within the optimized range

TABLE VII

PERFORMANCE OF TURNING LOCOMOTION

Model	**Rightward turn**			**Leftward turn**		
	Turn radius [cm]			**Turn radius** [cm]		
	40	50	60	40	50	60
	Angular speed per turn radius [rad/ms]					
Quadruped PyBullet model	2.36	1.64	1.16	2.27	1.57	1.11
Quadruped prototype	1.99	1.40	1.02	1.92	1.36	0.99
Error [%]	15.7	14.9	12.5	15.4	13.3	10.5

of trajectory parameters given in Table V. We initiated the testing at the pressure ceiling, 325 kPa, and the actuating frequency, 0.80 Hz since those gave stable locomotion for the straight motion (Sec. V-C). The testing was repeated for three amplitudes of turn radius ($\lambda = \{40, 50, 60\}$ cm) and leftward/rightward turn directions. During turning, we bend the robot body to accommodate differential turn radii on inward and outward limbs (Sec. III-C). It causes to increase in the active DoF of the quadruped from 12 (straight motion) to 15 (turning). Because of that, the quadruped turning showed relatively unsteady locomotion compared to its straight motion. Figure 10B visualizes the progression of the rightward turning at a turn radius, 40 cm and Table VII provides turning performances. For every gait, the robot’ s angular speed in relation to its turn radius was estimated using the method described for straight motion in Sec. V-C. The results show that the quadruped leverages its body bending to effectively turn while moving similar to its counterpart, PyBullet model. When the turn radius is low, the quadruped efficiently turned recording a higher angular speed per turn radius.

E. Discussion and Limitations

Note that, even though the quadruped PyBullet model showed locomotion stability within specific regions of trajectory parameters at all times, the quadruped prototype did not perform similarly due to its operational limitations and unaccounted characteristics. Limb characteristics such as deadzone, hysteresis of PMAs, etc. were not included in the soft limb PyBullet model, but were inherently included in the soft limb prototype. Additionally, pressure arrival onto PMAs is not consistent since long pressure supply tubes cannot transmit fast pressure changes in real-time.

There exists slight discrepancies between the dynamic responses of the PyBullet dynamic model and the experimental results of the robot prototype. For instance, the heel contact of the PyBullet model appears as a point contact whereas, in the robot prototype, it appears as distributed contact even though the results closely agree with each other. This is owing to the fact that soft robots (such as the soft limbs herein) can conform to the environment to find stability. Further, soft robots have a higher stability margin or error tolerance than the continuum limbs modeled through rigid body approximations in PyBullet. Because of such reasons, the robot prototype showed a slightly higher oscillatory behavior in each trotting cycle than the PyBullet model. These discrepancies are reflected by the error margins recorded in Tables VI and VII.

Testing on uneven terrains revealed that the quadruped’ s locomotion was less stable than on flat terrains. This can be attributed to the application of optimized trajectory parameters derived from flat terrain simulations to unstructured environments. PyBullet’ s limitations in simulating such environments further compounded this issue. Such variations in robot morphology or operational conditions necessitate precise parameter tuning to maintain stability and performance. Implementing a closed-loop control system was identified as a critical step for improving the maneuverability of model parameters and preserving desired limb morphology under dynamic conditions.

Prolonged actuator use revealed signs of fatigue, with soft limbs detaching from the body due to fatigue failure at 3D-printed joints. Furthermore, PMAs tend to develop air leaks at the wrappings after extended operation. These failure cases emphasize the need for designing more robust actuators. Additionally, preparing the quadruped framework for real-world deployment requires achieving untethered operation through onboard power and sensing, integrated with a feedback control system. This effort involves optimizing computational pipelines, utilizing lightweight control algorithms, and improving sensor fusion techniques to ensure efficient and reliable performance.

F. Estimate Energy Consumption

We examined the energy consumption during prototype testing of the trotting locomotion and contrasted it with the conventional crawling gait of the robot presented in our previous work [39] (refer to Movie 06 in the supplementary file). When the robot is powered by pneumatic pressure, P_{in} [Nm^{-2}], and its volumetric air flow rate, $\dot{V}$ [$m^3 s^{-1}$], the power output of the pneumatic system can be computed as $P_{in}\dot{V}$ [W]. Consequently, the energy expended by the pneumatic system (or the energy input to the robot), denoted as E, is determined by (26), with t representing the duration of robot actuation.

$$E = \int_0^t P_{in}\dot{V}dt. \tag{26}$$

To gauge the input air pressure and volumetric flow rate, a pressure sensor (PSE530-R07-L, SMC USA) and a flow sensor (PFM711-C6-E-M, SMC USA) are connected in series at the shared air inlet of pressure regulators as shown in Figs. 8A and 8B. An analog input DAQ card (PCI-6255, NI USA) is linked to the MATLAB Simulink desktop real-time model for obtaining sensor data, which manifests as voltage signals.

First, we actuated the robot to trot over a fixed straight distance of 3.0 m on flat terrain on flat terrain using the optimized trajectory parameters, recording the pressure input, air flow rate, and traverse time. Next, we repeated this procedure on sloped and naturalistic irregular terrains. Subsequently, we conducted the same experiment for trotting under various combinations of non-optimized trajectory parameters, as listed in column 2 of Table VIII, to investigate the effect of trajectory optimization on energy consumption. Therein, we isolated actuation frequency, f, and duty cycle, D, as variable non-optimized trajectory parameters since their impact

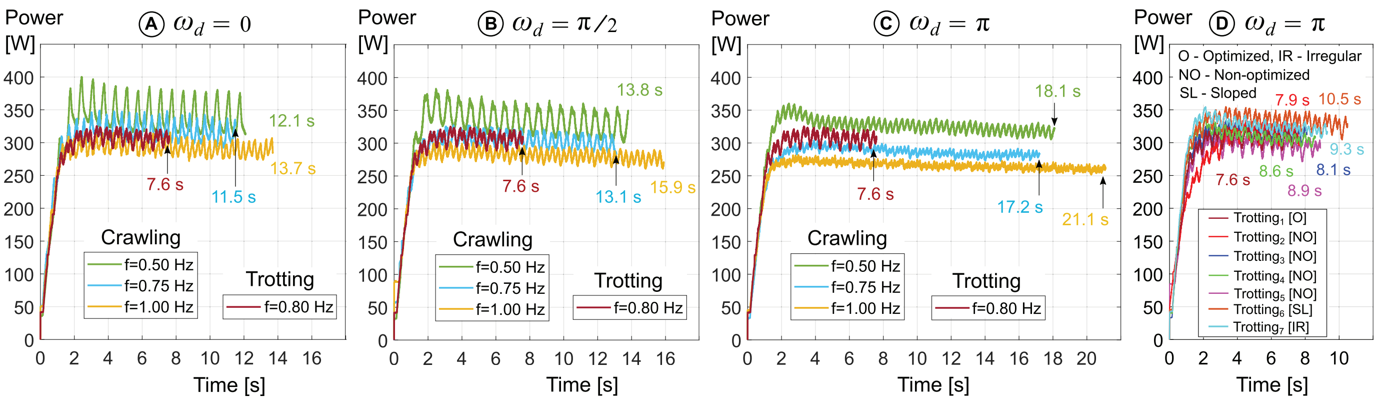

Fig. 12. Power output of the pneumatic system at phase gaits; (A) $\omega_d = 0$, (B) $\omega_d = \frac{\pi}{2}$ and, (C) $\omega_d = \pi\ rad$ under different actuation frequencies for crawling and optimized trotting gaits. (D) Power output of optimized and non-optimized trotting gaits on flat, sloped, and naturalistic irregular terrains. Here "optimized" refers to the one that gives the most stable locomotion and "Non-optimized" refers to the ones that give unstable locomotion.

TABLE VIII

ENERGY ESTIMATION IN TROTTING GAITS

Trotting type	**Optimized/ Non-optimized gait parameters**	**Energy consumption** $[KJ]$
Trotting$_1$ [O]	$f = 0.8\ Hz,\ D = 0.20$	2.14
Trotting$_2$ [NO]	$f = 0.8\ Hz,\ D = 0.15$	2.23
Trotting$_3$ [NO]	$f = 0.8\ Hz,\ D = 0.25$	2.19
Trotting$_4$ [NO]	$f = 0.9\ Hz,\ D = 0.20$	2.49
Trotting$_5$ [NO]	$f = 0.7\ Hz,\ D = 0.20$	2.57
Trotting$_6$ [SL]	$f = 0.8\ Hz,\ D = 0.20$	2.89
Trotting$_7$ [IR]	$f = 0.8\ Hz,\ D = 0.20$	2.73

O - Optimized, NO - Non-optimized, SL - Sloped, IR - Irregular

TABLE IX

ENERGY ESTIMATION IN CRAWLING GAITS

Actuating frequency $[Hz]$	**Phase shift in crawling gait** $[rad]$		
	$\omega_d = 0$	$\omega_d = \pi/2$	$\omega_d = \pi$
	Energy consumption $[KJ]$		
0.50	3.89	4.40	5.70
0.75	3.46	3.80	4.75
1.00	3.85	4.34	5.47

was significant for stability based on simulation results in Sec. IV-C.

Finally, we repeated the same step for crawling under identical conditions. The prior work in [39] demonstrated crawling under 9 phase shifts $\left(\omega_d \in \left\{0, \frac{\pi}{6}, \frac{\pi}{4}, \frac{\pi}{3}, \frac{\pi}{2}, \frac{2\pi}{3}, \frac{3\pi}{4}, \frac{5\pi}{6}, \pi\right\}\ rad\right)$ between diagonal limb pairs and 3 actuation frequencies ($f \in \{0.5, 0.75, 1.0\}\ Hz$). In this work, for estimating the energy consumption during crawling, we opted for lower, middle, and upper bounds of $\omega_d \in \left\{0, \frac{\pi}{2}, \pi\right\}\ rad$ along with the same actuation frequencies as representative boundary points. Table IX gives the computed energy output under each crawling gait.

Figures 12A, 12B, and 12C depict the power outputs of the pneumatic system (equivalent to the power input to the robot) based on (26) for crawling and optimized trotting gaits. Figure 12D compares the power output of optimized (most stable) and non-optimized (unstable) trotting gaits on flat, sloped, and naturalistic irregular terrains. When these results are combined with the estimated energy consumption in Table VIII, it is evident that both higher ($f = 0.9\ Hz$) and lower ($f = 0.7\ Hz$) actuation frequencies cause higher energy consumption compared to the optimized actuation frequency ($f = 0.8\ Hz$). The reason for this is that at lower actuation rates, the robot spends more time covering a fixed distance, resulting in prolonged operation of the pneumatic system. Conversely, at higher rates, the trajectory becomes distorted, making it difficult for the robot to cover the distance efficiently.

G. Analyze Locomotion Energy Efficiency

Figure 12 indicates that the robot dedicates a considerably lower duration to covering the specified fixed distance via trotting compared to crawling, regardless of the actuation frequency or limb phase shift of the crawling. Consequently, the data presented in Tables VIII and IX demonstrates that trotting consistently records a reduced energy input to the robot compared to crawling. The trotting has a smaller duty cycle than crawling, hence its floor contacts are minimal. Conversely, owing to the increased number of distributed floor contacts, crawling demands a significant amount of energy to overcome friction. We computed the energy efficiency of trotting relative to crawling as

$$E_{saving}[\%] = \frac{E_{crawling} - E_{trotting}}{E_{crawling}} \times 100. \qquad (27)$$

Table X provides a summary of the energy efficiencies for both optimized and non-optimized gaits across flat, sloped, and naturalistic irregular terrains. The results demonstrate that optimized trotting consistently saves the maximum percentage of energy compared to non-optimized conditions at all times. Accordingly, the optimized-trotting approximately saves energy, on average, 42 %, 48 %, and 59 % under phase shifts, 0, $\pi/2$, and π, respectively. The data aligns with the observation that the energy consumption of crawling increases as the phase shift, ω_d rises from 0 to π. The crawling reported in [39] demonstrated that higher ω_d values lead to lower speeds (see crawling videos in Movie 06). Therefore, because of the prolonged operating time of the pneumatic system, higher ω_d s have resulted in increased energy expenditure, thereby contributing to higher energy savings in trotting. Additionally,

TABLE X

ENERGY SAVING OF TROTTING AGAINST CRAWLING

Trotting type	**Phase shift in crawling gait** [rad]								
	$\omega_d = 0$			$\omega_d = \pi/2$			$\omega_d = \pi$		
	Freq. [Hz]			**Freq.** [Hz]			**Freq.** [Hz]		
	0.50	0.75	1.00	0.50	0.75	1.00	0.50	0.75	1.00
	Energy saving - E_{saving} [%]								
Trotting$_1$ [O]	45.0	38.2	44.4	51.4	43.7	50.7	62.5	54.9	60.9
Trotting$_2$ [NO]	42.7	35.5	42.1	49.3	41.3	48.6	60.9	53.1	59.2
Trotting$_3$ [NO]	43.7	36.7	43.1	50.2	42.4	49.5	61.6	53.9	59.8
Trotting$_4$ [NO]	36.0	28.0	35.3	43.4	34.5	42.6	56.3	47.6	54.5
Trotting$_5$ [NO]	33.9	25.7	33.2	41.6	32.4	40.8	54.9	45.9	53.0
Trotting$_6$ [SL]	25.7	16.5	24.9	34.3	23.9	33.4	49.3	39.2	47.2
Trotting$_7$ [IR]	29.8	21.1	29.1	38.0	28.2	37.1	52.1	42.5	50.1

the quadruped consumes slightly more energy while trotting on sloped and naturalistic irregular terrains compared to flat terrain. This is because negotiating sloped or irregular surfaces takes more time to cover the fixed distance, as evidenced by the power consumption recorded in Fig. 12D.

We also conducted a comparative analysis of the energy efficiencies of state-of-the-art quadrupedal locomotion approaches using the mechanical Cost of Transportation (CoT) metric, as described in [58]. Under optimal conditions, our quadruped achieved a CoT of 0.38 in unstructured terrain, demonstrating CoT reductions of 86.0 %, 84.6 %, and 13.5 % compared to the modern quadrupedal robots reported in [59], [60], and [61], respectively.

VI. CONCLUSION

We proposed dynamically-stable locomotion on a soft quadruped robot made of five identical soft modules (four limbs and a body). We detailed the soft limb design and the quadruped topology. Curve parametric limb kinematics were employed to parameterize a primitive trajectory profile and obtain quadrupedal locomotion trajectories for straight and turning motions. We developed a quadruped simulation model in the Bullet physics engine and optimized trajectory parameters to obtain fast walking (i.e., trotting) gaits. Next, the quadruped prototype was experimentally tested by applying optimized trajectory parameters. We compared the experimental results with the simulation results and evaluated the model performance. Both quadruped models showed similar locomotion performance. The quadruped achieved trotting at a peak speed of 1.24 body lengths per second and a peak angular speed of 1.99 *rad* per turn radius per second when traversing flat and uneven terrains, including slopes, cluttered areas, and naturalistic irregular surfaces. Our work demonstrated that a virtual environment that supports physics-based interactions can be employed to realize dynamically-stable locomotion in soft robots. In the end, our energy cost analysis revealed that trotting is a more energy-efficient mode of locomotion, yielding an average energy saving of up to 42% compared to traditional quadrupedal locomotion modes such as crawling.

Our future research will focus on enhancing autonomy through onboard power and sensing, closed-loop control, and advanced path planning. We aim to achieve untethered operation by transitioning to electromechanical actuation, which will involve redesigning hybrid soft modules. We will also explore new locomotion modes, such as discontinuous gaits, to expand the quadruped' s capabilities.

REFERENCES

[1] F. Schmitt, O. Piccin, L. Barbé, and B. Bayle, "Soft robots manufacturing: A review," *Frontiers Robot. AI*, vol. 5, p. 84, Jul. 2018.

[2] E. W. Hawkes, L. H. Blumenschein, J. D. Greer, and A. M. Okamura, "A soft robot that navigates its environment through growth," *Sci. Robot.*, vol. 2, no. 8, Jul. 2017, Art. no. eaan3028.

[3] B. Mazzolai et al., "Roadmap on soft robotics: Multifunctionality, adaptability and growth without borders," *Multifunctional Mater.*, vol. 5, no. 3, Sep. 2022, Art. no. 032001.

[4] C. Laschi, J. Rossiter, F. Iida, M. Cianchetti, and L. Margheri, *Soft Robotics: Trends, Applications and Challenges*, vol. 17. Cham, Switzerland: Springer, 2017.

[5] S. Chen et al., "Soft crawling robots: Design, actuation, and locomotion," *Adv. Mater. Technol.*, vol. 5, no. 2, Feb. 2020, Art. no. 1900837.

[6] M. Calisti, G. Picardi, and C. Laschi, "Fundamentals of soft robot locomotion," *J. Roy. Soc. Interface*, vol. 14, no. 130, May 2017, Art. no. 20170101.

[7] Y. Ansari, A. L. Shoushtari, V. Cacucciolo, M. Cianchetti, and C. Laschi, "Dynamic walking with a soft limb robot," in *Proc. Conf. Biomimetic Biohybrid Syst.* Cham, Switzerland: Springer, 2015, pp. 13–25.

[8] A. A. M. Faudzi, M. R. M. Razif, G. Endo, H. Nabae, and K. Suzumori, "Soft-amphibious robot using thin and soft Mckibben actuator," in *Proc. IEEE Int. Conf. Adv. Intell. Mechatronics (AIM)*, Jul. 2017, pp. 981–986.

[9] Y. Sun et al., "Soft mobile robots: A review of soft robotic locomotion modes," *Current Robot. Rep.*, vol. 2, no. 4, pp. 371–397, Dec. 2021.

[10] K. Suzumori, "Elastic materials producing compliant robots," *Robot. Auto. Syst.*, vol. 18, nos. 1–2, pp. 135–140, Jul. 1996.

[11] Z. Liu and K. Karydis, "Position control and variable-height trajectory tracking of a soft pneumatic legged robot," in *Proc. IEEE/RSJ Int. Conf. Intell. Robots Syst. (IROS)*, Sep. 2021, pp. 1708–1709.

[12] S. Li et al., "Scaling up soft robotics: A meter-scale, modular, and reconfigurable soft robotic system," *Soft Robot.*, vol. 9, no. 2, pp. 324–336, Apr. 2022.

[13] K. Hase, T. Akagi, S. Dohta, T. Shinohara, W. Kobayashi, and S. Shimooka, "Development of six-legged mobile robot using tetrahedral shaped pneumatic soft actuators," *JFPS Int. J. Fluid Power Syst.*, vol. 15, no. 1, pp. 33–39, 2022.

[14] D. M. Perera et al., "Teleoperation of soft modular robots: Study on real-time stability and gait control," in *Proc. IEEE Int. Conf. Soft Robot. (RoboSoft)*, Apr. 2023, pp. 01–07.

[15] D. D. K. Arachchige et al., "Study on soft robotic pinniped locomotion," in *Proc. IEEE/ASME Int. Conf. Adv. Intell. Mechatronics (AIM)*, Jun. 2023, pp. 65–71.

[16] D. D. K. Arachchige, D. M. Perera, U. Huzaifa, I. Kanj, and I. S. Godage, "Tumbling locomotion of tetrahedral soft-limbed robots," *IEEE Robot. Autom. Lett.*, vol. 9, no. 5, pp. 4337–4344, May 2024.

[17] P. Wharton et al., "Tetraflex: A multigait soft robot for object transportation in confined environments," *IEEE Robot. Autom. Lett.*, vol. 8, no. 8, pp. 5007–5014, Aug. 2023.

[18] Y. Li et al., "An untethered soft robotic dog standing and fast trotting with jointless and resilient soft legs," *Biomimetics*, vol. 8, no. 8, p. 596, Dec. 2023.

[19] J. Ketchum, S. Schiffer, M. Sun, P. Kaarthik, R. L. Truby, and T. D. Murphey, "Automated gait generation for walking, soft robotic quadrupeds," in *Proc. IEEE/RSJ Int. Conf. Intell. Robots Syst. (IROS)*, Oct. 2023, pp. 10245–10251.

[20] Z. Xiong, Y. Su, and H. Lipson, "Fast untethered soft robotic crawler with elastic instability," in *Proc. IEEE Int. Conf. Robot. Autom. (ICRA)*, May 2023, pp. 2606–2612.

[21] J. M. Bern, P. Banzet, R. Poranne, and S. Coros, "Trajectory optimization for cable-driven soft robot locomotion," in *Robotics: Science and Systems*, vol. 1, no. 3, 2019.

[22] M. Wu et al., "A fully 3D-printed tortoise-inspired soft robot with terrains-adaptive and amphibious landing capabilities," *Adv. Mater. Technol.*, vol. 7, no. 12, Dec. 2022, Art. no. 2200536.

[23] W. Zhong, Y. Wu, L. Li, J. Shao, and X. Gu, "A tortoise-inspired quadrupedal pneumatic soft robot that adapts to environments through shape change," *Bioinspiration Biomimetics*, Mar. 2025.

[24] X. Ai, H. Yue, and W. D. Wang, "Crawling soft robot exploiting wheel-legs and multimodal locomotion for high terrestrial maneuverability," *IEEE Trans. Robot.*, vol. 39, no. 6, pp. 4230–4239, Dec. 2023.

[25] B. Yang et al., "Self-amputating and interfusing machines," *Adv. Mater.*, vol. 36, no. 32, Aug. 2024, Art. no. 2400241.

[26] M. A. I. Kalin, C. Aygül, A. Türkmen, J. Kwiczak-Yigitbasi, B. Baytekin, and O. Özcan, "Design, fabrication, and locomotion analysis of an untethered miniature soft quadruped, SQuad," *IEEE Robot. Autom. Lett.*, vol. 5, no. 3, pp. 3854–3860, Jul. 2020.

[27] B. Xia, J. Fu, H. Zhu, Z. Song, Y. Jiang, and H. Lipson, "A legged soft robot platform for dynamic locomotion," in *Proc. IEEE Int. Conf. Robot. Autom. (ICRA)*, May 2021, pp. 11812–11819.

[28] L. Schiller, A. Seibel, and J. Schlattmann, "Toward a gecko-inspired, climbing soft robot," *Frontiers Neurorobotics*, vol. 13, p. 106, Dec. 2019.

[29] Q. Ji et al., "Synthesizing the optimal gait of a quadruped robot with soft actuators using deep reinforcement learning," *Robot. Comput.-Integr. Manuf.*, vol. 78, Dec. 2022, Art. no. 102382.

[30] J. Kim, E. Im, Y. Lee, and Y. Cha, "Quadrupedal robot with tendon-driven origami legs," *Sens. Actuators A, Phys.*, vol. 378, Nov. 2024, Art. no. 115769.

[31] Y. Kim, Y. Lee, and Y. Cha, "Origami pump actuator based pneumatic quadruped robot (OPARO)," *IEEE Access*, vol. 9, pp. 41010–41018, 2021.

[32] Y. Sun, F. Pancheri, C. Rehekampff, and T. C. Lueth, "TurBot: A turtle-inspired quadruped robot using topology optimized soft-rigid hybrid legs," *IEEE/ASME Trans. Mechatronics*, vol. 29, no. 4, pp. 3193–3202, Aug. 2024.

[33] A. N. M. A. Siddiquee and Y. Ozkan-Aydin, "Utilizing bioinspired soft modular appendages for grasping and locomotion in multi-legged robots on ground and underwater," *IEEE Robot. Autom. Lett.*, vol. 9, no. 4, pp. 3862–3869, Apr. 2024.

[34] M. Hongjun, Z. Shupeng, Z. Wei, and R. Yuke, "Design and control of a new pneumatic quadruped soft robot based on honeycomb structure," *IEEE Access*, vol. 12, pp. 98882–98899, 2024.

[35] X. Huang, K. Kumar, M. Khalid Jawed, Z. Ye, and C. Majidi, "Soft electrically actuated quadruped (SEAQ)—Integrating a flex circuit board and elastomeric limbs for versatile mobility," *IEEE Robot. Autom. Lett.*, vol. 4, no. 3, pp. 2415–2422, Jul. 2019.

[36] R. F. Shepherd et al., "Multigait soft robot," *Proc. Nat. Acad. Sci. USA*, vol. 108, no. 51, pp. 20400–20403, Dec. 2011.

[37] D. Drotman, S. Jadhav, D. Sharp, C. Chan, and M. T. Tolley, "Electronics-free pneumatic circuits for controlling soft-legged robots," *Sci. Robot.*, vol. 6, no. 51, Feb. 2021, Art. no. eaay2627.

[38] I. S. Godage, T. Nanayakkara, and D. G. Caldwell, "Locomotion with continuum limbs," in *Proc. IEEE/RSJ Int. Conf. Intell. Robots Syst.*, Oct. 2012, pp. 293–298.

[39] D. D. K. Arachchige, D. M. Perera, S. Mallikarachchi, U. Huzaifa, I. Kanj, and I. S. Godage, "Soft steps: Exploring quadrupedal locomotion with modular soft robots," *IEEE Access*, vol. 11, pp. 63136–63148, 2023.

[40] Q. Ji, S. Fu, L. Feng, G. Andrikopoulos, X. V. Wang, and L. Wang, "Omnidirectional walking of a quadruped robot enabled by compressible tendon-driven soft actuators," in *Proc. IEEE/RSJ Int. Conf. Intell. Robots Syst. (IROS)*, Oct. 2022, pp. 11015–11022.

[41] D. D. K. Arachchige and I. S. Godage, "Hybrid soft robots incorporating soft and stiff elements," in *Proc. IEEE 5th Int. Conf. Soft Robot. (RoboSoft)*, Apr. 2022, pp. 267–272.

[42] D. D. K. Arachchige, Y. Chen, I. D. Walker, and I. S. Godage, "A novel variable stiffness soft robotic gripper," in *Proc. IEEE 17th Int. Conf. Autom. Sci. Eng. (CASE)*, Aug. 2021, pp. 2222–2227.

[43] D. D. K. Arachchige, D. M. Perera, S. Mallikarachchi, I. Kanj, Y. Chen, and I. S. Godage, "Wheelless soft robotic snake locomotion: Study on sidewinding and helical rolling gaits," in *Proc. IEEE Int. Conf. Soft Robot. (RoboSoft)*, Apr. 2023, pp. 1–6.

[44] U. Huzaifa, D. D. K. Arachchige, M. A. U. Zaman, and U. Syed, "Simplified modeling of hybrid soft robots with constant stiffness assumption," in *Proc. IEEE Int. Conf. Robot. Biomimetics (ROBIO)*, Dec. 2023, pp. 1–6.

[45] B. H. Meng, D. D. K. Arachchige, I. S. Godage, and I. Kanj, "Path planning for continuum arms in dynamic environments," in *Proc. IEEE 7th Int. Conf. Soft Robot. (RoboSoft)*, Apr. 2024, pp. 900–905.

[46] D. M. Perera, N. Byrd, D. D. K. Arachchige, B. Vajipeyajula, K. C. Galloway, and I. S. Godage, "Curve parametric modeling of planar soft robots," in *Proc. IEEE Int. Conf. Mechatronics Autom. (ICMA)*, Aug. 2024, pp. 299–304.

[47] I. S. Godage, G. A. Medrano-Cerda, D. T. Branson, E. Guglielmino, and D. G. Caldwell, "Modal kinematics for multisection continuum arms," *Bioinspiration Biomimetics*, vol. 10, no. 3, May 2015, Art. no. 035002.

[48] A. Spröwitz, A. Tuleu, M. Vespignani, M. Ajallooeian, E. Badri, and A. J. Ijspeert, "Towards dynamic trot gait locomotion: Design, control, and experiments with cheetah-cub, a compliant quadruped robot," *Int. J. Robot. Res.*, vol. 32, no. 8, pp. 932–950, Jul. 2013.

[49] E. Coumans and Y. Bai. (2021). *PyBullet Quickstart Guide*. [Online]. Available: https://pybullet.org/wordpress/index.php/forum-2/

[50] E. Coumans and Y. Bai. (2016). *Pybullet, a Python Module for Physics Simulation*. [Online]. Available: http://pybullet.org

[51] H. Yin, A. Varava, and D. Kragic, "Modeling, learning, perception, and control methods for deformable object manipulation," *Sci. Robot.*, vol. 6, no. 54, May 2021, Art. no. eabd8803.

[52] I. S. Godage, R. Wirz, I. D. Walker, and R. J. Webster, "Accurate and efficient dynamics for variable-length continuum arms: A center of gravity approach," *Soft Robot.*, vol. 2, no. 3, pp. 96–106, Sep. 2015.

[53] H. Habibi, C. Yang, I. S. Godage, R. Kang, I. D. Walker, and D. T. Branson, "A lumped-mass model for large deformation continuum surfaces actuated by continuum robotic arms," *J. Mech. Robot.*, vol. 12, no. 1, Feb. 2020, Art. no. 011014.

[54] A. Amaya, D. D. K. Arachchige, J. Grey, and I. S. Godage, "Evaluation of human–robot teleoperation interfaces for soft robotic manipulators," in *Proc. 30th IEEE Int. Conf. Robot Hum. Interact. Commun. (RO-MAN)*, Aug. 2021, pp. 412–417.

[55] (2024). *MATLAB Engine Api for Python*. [Online]. Available: https://pypi.org/project/matlabengine/

[56] D. D. K. Arachchige et al., "Dynamic modeling and validation of soft robotic snake locomotion," in *Proc. 9th Int. Conf. Control, Autom. Robot. (ICCAR)*, Apr. 2023, pp. 6–12.

[57] D. D. K. Arachchige, Y. Chen, and I. S. Godage, "Soft robotic snake locomotion: Modeling and experimental assessment," in *Proc. IEEE 17th Int. Conf. Autom. Sci. Eng. (CASE)*, Aug. 2021, pp. 805–810.

[58] T. J. K. Buchner et al., "Electrohydraulic musculoskeletal robotic leg for agile, adaptive, yet energy-efficient locomotion," *Nature Commun.*, vol. 15, no. 1, p. 7634, Sep. 2024.

[59] G. Bravo-Palacios, H. Li, and P. M. Wensing, "Engineering compliance in legged robots via robust co-design," *IEEE/ASME Trans. Mechatronics*, vol. 29, no. 6, pp. 4711–4722, Dec. 2024.

[60] L. Wei et al., "Economical quadrupedal multi-gait locomotion via gait-heuristic reinforcement learning," *J. Bionic Eng.*, vol. 21, no. 4, pp. 1720–1732, Jul. 2024.

[61] S. Li et al., "Learning locomotion for quadruped robots via distributional ensemble actor-critic," *IEEE Robot. Autom. Lett.*, vol. 9, no. 2, pp. 1811–1818, Feb. 2024.

Dimuthu D. K. Arachchige received the B.Sc. degree in mechanical engineering from the University of Ruhuna, Sri Lanka, in 2008, the M.Sc. degree in renewable energy from the University of Agder, Norway, in 2014, the M.Sc. degree in electronics and automation from the University of Moratuwa, Sri Lanka, in 2017, and the Ph.D. degree in computer science from the DePaul University, USA, in 2024. During his doctoral studies, his research focused on soft modular robotics. He is currently a Post-Doctoral Researcher with the Rehabilitation Robotics Laboratory, Department of Mechanical and Industrial Engineering, University of Illinois at Chicago, USA.

Tim Sheehan received the B.S. degree in computer science, major in cyber-physical systems engineering from DePaul University, Chicago, IL, USA, in 2021. During his undergraduate period, he was with the Robotics and Medical Engineering Laboratory, School of Computing, Jarvis College of Computing and Digital Media, DePaul University, and worked in the area of soft modular robotics. He is currently a Web Developer with Americaneagle.com Inc.

Dulanjana M. Perera (Graduate Student Member, IEEE) received the B.Sc. and M.Sc. degrees in mechanical engineering from the University of Moratuwa, Sri Lanka, in 2018 and 2021, respectively. He is currently pursuing the Ph.D. degree in interdisciplinary engineering with Texas A&M University, College Station, TX, USA. He is also a Graduate Teaching Assistant of Electronic Systems Engineering with the Department of Engineering Technology and Industrial Distribution, Texas A&M University. His current research interests include soft modular robot control and machine learning.

Sanjaya Mallikarachchi (Graduate Student Member, IEEE) received the B.Sc. degree in mechanical engineering from the University of Moratuwa, Sri Lanka, in 2018, and the M.S. degree in computer science from DePaul University, USA, in 2023. He is currently pursuing the Ph.D. degree in interdisciplinary engineering with Texas A&M University, College Station, TX, USA. He is also a Graduate Teaching Assistant of Electronic Systems Engineering with the Department of Engineering Technology and Industrial Distribution, Texas A&M University. His research interests are robotics, mechatronics, and automation.

Umer Huzaifa received the M.S. and Ph.D. degrees in mechanical engineering from the University of Illinois at Urbana–Champaign, USA, in 2016 and 2019, respectively. He is currently an Assistant Professor of Cyber-Physical Systems Engineering with DePaul University, USA, where he is investigating robot locomotion and novel devices for assisting human movement. He was a Finalist of the Best Poster Award at the 2016 IEEE RAS/EMBS International Conference on Biomedical Robotics & Biomechatronics (BioRob).

Iyad Kanj received the B.Sc. degree in computer science from American University of Beirut in 1995 and the Ph.D. degree in computer science from Texas A&M University in 2001. He is currently a Professor of Computer Science with the School of Computing, Jarvis College of Computing and Digital Media, DePaul University, Chicago, IL, USA. His research interests include parameterized complexity, graph theory and algorithms, combinatorial optimization, computational geometry, and robot path planning.

Isuru S. Godage received the B.Sc. degree in electronic and telecommunication engineering from the University of Moratuwa, Sri Lanka, in 2007, and the Doctorate degree in robotics, cognition, and interaction technologies from Italian Institute of Technology—University of Genova, Italy, in 2013. He was an Assistant Professor with DePaul University, USA; and a Post-Doctoral Fellow with Vanderbilt University, USA, and Clemson University, USA. He is currently an Assistant Professor with the Department of Engineering Technology and Industrial Distribution, J. Mike Walker ’66 Department of Mechanical Engineering (affiliated) and Department of Multidisciplinary Engineering (affiliated), Texas A&M University, College Station, TX, USA. His research interests are soft modular robotics, surgical robotics, modeling and analysis of continuum structures, and underactuated system control/coordination through energy-based methods.